

pubs.acs.org/cm Article

Cascade of Phase Transitions and Large Magnetic Anisotropy in a Triangle-Kagome-Triangle Trilayer Antiferromagnet

Chao Liu, Tieyan Chang, Shilei Wang, Shun Zhou, Xiaoli Wang, Chuanyan Fan, Lu Han, Feiyu Li, Huifen Ren, Shanpeng Wang, Yu-Sheng Chen, and Junjie Zhang*



Cite This: Chem. Mater. 2024, 36, 9516–9525



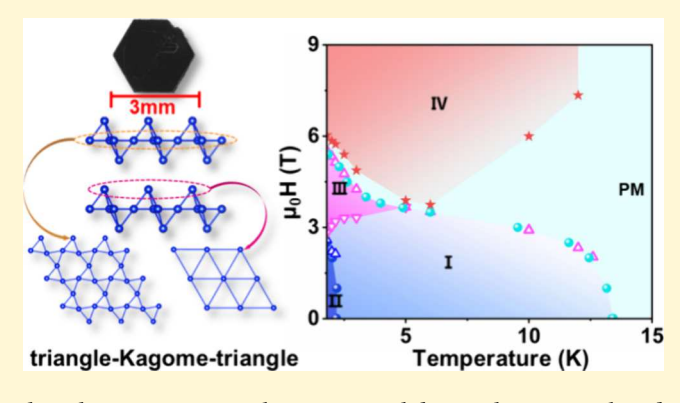
ACCESS I

III Metrics & More

Article Recommendations

s Supporting Information

ABSTRACT: Spins in strongly frustrated systems are of intense interest due to the emergence of intriguing quantum states including superconductivity and quantum spin liquid. Herein, we report the discovery of a cascade of phase transitions and large magnetic anisotropy in the averievite $CsClCu_5P_2O_{10}$ single crystals. Under a zero field, $CsClCu_5P_2O_{10}$ undergoes a first-order structural transition at around 224 K from high-temperature centrosymmetric P3m1 to low-temperature noncentrosymmetric P321 followed by an AFM transition at 13.6 K, and another AFM transition at ~ 2.18 K. Based upon magnetic susceptibility and magnetization data with magnetic fields perpendicular to the ab plane, a phase diagram, consisting of a paramagnetic state, two AFM states, and two field-induced states including two magnet-



ization plateaus, has been constructed. Our findings demonstrate that the quasi-2D $CsClCu_5P_2O_{10}$ exhibits rich structural and metamagnetic transitions, and the averievite family is a fertile platform for exploring novel quantum states.

■ INTRODUCTION

Understanding the origin of high-temperature superconductivity remains a big challenge and is among the current research frontiers. 1-3 Nearly 40 years ago, Anderson proposed that the pre-existing magnetic singlet pairs of quantum spin liquid (QSL), which is an insulating magnetic state favored by low spin, low dimensionality, and magnetic frustration,4 could become charged superconducting pairs when it is doped sufficiently strongly.⁵ Anderson's theory has not been tested up to now.^{6–9} The main obstacle is that no existing materials have been confirmed to be QSL due to the lack of smoking-gun evidence; only a few materials are proximate QSL candidates, including k-(ET)₂Cu₂(CN)₃, herbertsmithite ZnCu₃(OH)₆Cl₂, and α -RuCl₃.^{7,11,12} Herbertsmithite, which does not show any long-range magnetic order or spin glass behavior down to 20 mK, $^{13-15}$ is probably one of the most studied QSL candidates. Theoretically, electron doping with Ga on the Zn site in herbertsmithite was predicted to produce novel states including f-wave superconductivity and a correlated Dirac metal, 16 and hole doping with Li or Na on the Zn site was predicted to host a fractional quantum Hall effect. 17 Experimentally, attempts to dope electrons/holes by substitution via various techniques in this material ended in unsuccess; one reason is that the removal of Zn from the threedimensional (3D) crystal structure leads to decomposition. 15,18 One notable progress was the report of lithium intercalation in herbertsmithite; however, this did not lead to metallization,

not to mention superconductivity.¹⁹ Thus, it is desirable to find other QSL candidates that maintain the key ingredients of herbertsmithite (kagome lattice with $Cu^{2+}S = 1/2$) but do not have its issues.

Geometrically frustrated systems such as triangular, honeycomb, kagome, hyperkagome, and pyrochlore are fertile playgrounds for the exploration of novel quantum phases including quantum spin liquid.8 Averievite, an oxide mineral represented by the formula $(MX)_n Cu_5 T_2 O_{10}$ (M = K, Rb, Cs,Cu; X = Cl, Br, I; n=1; T = P, $V^{n_{20}-23}$ that contains tranglekagome-triangle trilayers of Cu^{2+} (S = 1/2), is a geometrically frustrated system and has been proposed to host QSL.²⁴ More importantly, unlike the 3D network in herbertsmithite,²⁵ averievite exhibits a quasi-2D crystal structure consisting of triangle-kagome-triangle trilayers of Cu and MO2 layers between them, potentially overcoming the doping issues encountered in herbertsmithite. $CsClCu_5V_2O_{10}$ polycrystalline powders were reported to crystallize in the $P\overline{3}m1$ space group at high temperatures and undergoes a structural transition to $P2_1/c$ at 310 K and then to an unknown structure below 127 K

Received: May 8, 2024
Revised: September 9, 2024
Accepted: September 9, 2024
Published: September 28, 2024





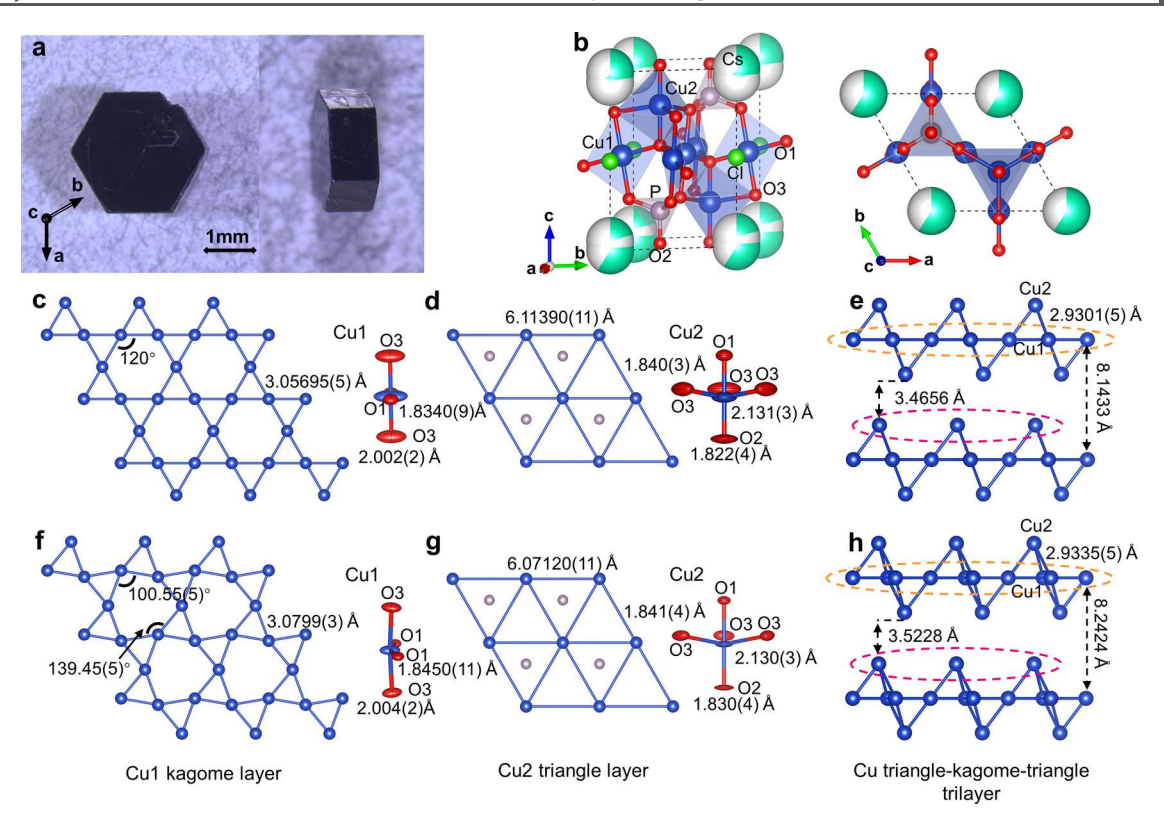


Figure 1. Single crystals and crystal structures of $CsClCu_5P_2O_{10}$ from synchrotron X-ray single crystal diffraction. (a) Photos of a typical piece of an as-grown single crystal, (b) crystal structure of $CsClCu_5P_2O_{10}$ at 300 K in the ball-and-stick model, (c) kagome layer consisting of the Cu1 at 300 K and Cu1 local environment in the ellipsoid model, (d) triangle layer consisting of Cu2 with P atoms residing in the middle of Cu triangles at 300 K and the Cu2 local environment in the ellipsoid model, (e) triangle-kagome-triangle trilayer at 300 K, (f) distorted kagome layer consisting of the Cu1 at 100 K and Cu1 local environment in the ellipsoid model, (g) triangle layer consisting of the Cu2 at 100 K and Cu2 local environment in the ellipsoid model, and (h) triangle-kagome-triangle trilayer at 100 K.

followed by an antiferromagnetic transition at 24 K.24 In contrast, Kornyakov et al. reported a four-time large unit cell with a $P\overline{3}$ space group at 296 K.²⁰ By substituting 20% Cu with Zn to form CsClCu₄ZnV₂O₁₀, polycrystalline powders did not show conventional magnetic order or spin glass behavior down to 1.8 K.^{24,26} Theoretical calculations predicted that the further doped averievite CsClCu₃Zn₂V₂O₁₀ is a QSL candidate.²⁴ Moving from V to P, it was reported that the antiferromagnetic transition T_N of CsClCu₅P₂O₁₀ powders was suppressed to 3.8 K and the structural transition was shifted to 12 K.²¹ Theoretical calculations revealed that substitution of V by P in averievite causes chemical pressure, leading to stronger interlayer coupling between Cu kagome and Cu triangle atoms and larger degree of magnetic frustration.²⁷ To address the existing key fundamental questions including the temperaturedependent crystal structure, whether Zn-doped averievites are QSL candidates, and the direction-dependent physical properties, bulk single crystals are highly demanded; however, up to date, only submillimeter-sized single crystals of averievite $CsClCu_5V_2O_{10}$ (0.42 × 0.40 × 0.05 mm³) and $CsClCu_5P_2O_{10}$ $(0.12 \times 0.12 \times 0.03 \text{ mm}^3)$ have been reported.²⁰

In this contribution, we report the successful growth of $CsClCu_5P_2O_{10}$ single crystals with dimensions of 3–5 mm on edge (Figure 1a) using a flux method. The availability of bulk $CsClCu_5P_2O_{10}$ single crystals not only promotes structural study across first-order transitions but also provides an ideal platform for measurements of direction-dependent physical properties for a deep understanding of this averievite. Combining synchrotron powder X-ray diffraction and single

crystal diffraction, we report a previously unidentified first-order structural transition at 224 K₂ transforming from the high-temperature centrosymmetric P3m1 to low-temperature noncentrosymmetric P321 space group. Such a transition was corroborated by a pair of peaks in the differential scanning calorimetry curves, an anomaly in heat capacity and thermal hysteresis between warming and cooling in magnetic susceptibility. Strong anisotropic magnetic properties were observed for the first time in averievite. A magnetic phase diagram, consisting of a paramagnetic state, two antiferromagnetic states, and two field-induced states, has been constructed based upon the magnetic susceptibility and magnetization data with magnetic fields perpendicular to the ab plane. Our findings suggest that quasi-2D $CsClCu_sP_2O_{10}$ is an excellent platform for exploring novel quantum states.

■ MATERIALS AND METHODS

Crystal Growth. Single crystals of $CsClCu_5P_2O_{10}$ were grown using a flux method for the first time in sealed quartz tubes. CuO (Macklin, AR), $Cu_2P_2O_7$ · H_2O (Macklin, 99.99%), and CsCl (Macklin, AR) were weighed with a molar ratio of 3:1:1 and then mixed with flux in a mass ratio of 1:5 where the flux is $CsCl/CuCl_2 = 7:3$ (mass ratio). The $CuCl_2$ was obtained by preheating $CuCl_2$ · $2H_2O$ (Aladdin, AR) at 150 °C for 12 h. The mixture was loaded into a quartz tube, sealed, then heated to 600 °C, held at this temperature for 1 day, and then cooled to 400 °C at a rate of 2 °C/h followed by furnace cooling to room temperature. Black hexagonal single crystals were obtained after removing flux using deionized water. Figure 1a shows a typical hexagonal black $CsClCu_5P_2O_{10}$ single crystal with dimensions of $3.12 \times 2.86 \times 0.97$ mm³ grown from $CsCl/CuCl_2$ flux.

The directions of the as-grown single crystals were determined by using X-ray diffraction (Figure S1).

Synchrotron X-ray Single Crystal Diffraction (SXRD). SXRD data were collected with a 1 M Pilatus area detector using synchrotron radiation ($\lambda = 0.41328 \text{ Å}$) at 300, 200, 100, and 6 K at Beamline 15-ID-D (NSF's ChemMatCARS) at the Advanced Photon Source, Argonne National Laboratory. The data collected at 300, 200, and 100 K are from the same single crystal (sample #1), while the data collected at 6 K are from another single crystal (sample #2). Single crystals were mounted to the tip of glass fiber and measured using a Huber 3-circle diffractometer. Indexing, data reduction, and image processing were performed using Bruker APEX4 software. 28 The structure was solved by direct methods and refined with full matrix least-squares methods on F2. All atoms were modeled using anisotropic ADPs, and the refinements converged for $I > 2\sigma(I)$ where I is the intensity of reflections and $\sigma(I)$ is the standard deviation. Calculations were performed using the SHELXTL crystallographic software package.²⁸ Details of crystal parameters, data collection, and structure refinement at 300, 200, 100, and 6 K are summarized in Table S1, and selected bond lengths (Å) and angles (deg) are presented in Table S2. Further details of the crystal structure investigations may be obtained from the joint CCDC/FIZ Karlsruhe online deposition service by quoting the deposition numbers CSD 2263860, 2263800, 2263806, and 2263799.

In-house X-ray Powder Diffraction (PXRD). In-house X-ray powder diffraction was carried out on a Bruker AXS D2 Phaser X-ray powder diffractometer. Pulverized $CsClCu_5P_2O_{10}$ single crystals were measured at room temperature using $Cu\ K\alpha$ radiation ($\lambda=1.5418\ \text{Å}$) in the 2θ range of $5-70^\circ$ with a scan step size of 0.02° and a scan time of $0.1\ s$ per step.

High-Resolution Synchrotron X-ray Powder Diffraction (HRPXRD). High-resolution synchrotron X-ray powder diffraction data of $CsClCu_5P_2O_{10}$ were collected in the 2θ range of $0.5-50^{\circ}$ with a step size of 0.001° and a step time of 0.1 s at 100, 200, and 295 K with an X-ray wavelength of $\lambda = 0.45903$ Å at Beamline 11-BM at the Advanced Photon Source, Argonne National Laboratory. Samples were prepared by loading pulverized crystals into an Φ 0.8 mm Kapton capillary, which was then installed on a magnetic sample base used by the beamline sample changer. The sample was spun continuously at 5600 rpm during data collection. An Oxford Cryostream 700 Plus N2 gas blower was used to control temperature below room temperature. Diffraction patterns were recorded on warming, first at 100 K and then at 200 and 295 K. Data were analyzed with the Rietveld method using GSAS-II software.² structures from SXRD were used as starting models, and the refined parameters include scale, background, unit cell parameters, domain size, microstrain, atomic positions, and thermal parameters. Isotropic domain sizes and generalized microstrain models were used.

Differential Scanning Calorimetry (DSC). DSC was used to check whether there was any structural phase transition in $CsClCu_5P_2O_{10}$. Data between 113 and 353 K was collected on a Mettler Toledo TGA/DSC3+ with 28.03 mg of $CsClCu_5P_2O_{10}$ pulverized crystals placed in an Al pan at a rate of 10 K/min on warming/cooling.

Heat Capacity (C_p). C_p of C_p ColCu₅ P_2O_{10} was obtained on a Quantum Design PPMS in a temperature range of 2–20 K. For single crystal measurement (5.9 mg), Apiezon-N vacuum grease was employed to fix crystals to the sapphire sample platform. The specific heat contribution from the sample holder platform and grease was determined before mounting the sample and subtracted from the total heat capacity. For powder measurement, a piece of single crystal (\sim 1 mg) was ground into powder, mixed with N grease, and then transferred to a sample stage. Data was collected between 19.8 and 1.8 K with a step size of 0.1 K.

Magnetic Susceptibility. DC and AC magnetic susceptibility data of $CsClCu_3P_2O_{10}$ using a single crystal of 16.4 mg were collected using a Quantum Design MPMS3 instrument at the Synergetic Extreme Condition User Facility (SECUF), Institute of Physics, Chinese Academy of Sciences. For a magnetic field perpendicular to the ab plane $(\mu_0H\perp ab)$, the crystal sandwiched between two quartz

was then inserted and fixed in a brass tube. ZFC-W (zero-field cooling, data collection on warming), FC-C (field cooling, data collection on cooling), and FC-W (field cooling, data collection on warming) were collected between 1.8 and 30 K with a heating rate of 3 K/min under an external magnetic field of 0.001, 0.01, 1.0, 2.0, 2.5, 3.0, 3.5, 3.65, 3.8, 4.0, 4.5, 5.0, 5.4, and 7.0 T, respectively. Magnetization data as a function of the magnetic field were collected between -7 to +7 T with a sweep mode of 150 Oe/s at 1.8, 2.15, 2.5, 6.0, 10.0, 12.6, 13.6, and 15.0 K. For the magnetic field parallel to the ab plane $(\mu_0 H || ab)$, the hexagonal surface of the crystal was attached to the plane of semicircular quartz columns by using GE varnish. ZFC-W, FC-C, and FC-W data were collected between 1.8 and 30 K, and the heating rate was 3 K/min under magnetic fields of 0.001, 0.01, and 1.0 T. AC magnetic data was collected between 8.8 and 9 K with a step size of 0.02 K at 10, 97, 497, 747, and 997 Hz. The Quantum Design PPMS Dynacool-9 was used to measure the DC magnetic susceptibility of CsClCu₅P₂O₁₀ single crystals between 2 and 300 K for a magnetic field perpendicular to the ab plane and parallel to the ab plane. ZFC-W, FC-C, and FC-W data were collected using the sweep mode with a heating rate of 3 K/min under a magnetic field of 2000 Oe. Magnetization vs magnetic field data was collected between -9 and +9 T using the sweep mode with a rate of 150 Oe/s at 2.0, 3.0, 5.0, 10.0, 12.0, 15.0, 20.0, 30.0, and 300 K. Measurements on other single crystals were performed to confirm the magnetic properties of the material (Figure S2).

■ RESULTS AND DISCUSSION

Crystal Structure. The crystal structure of CsClCu₅P₂O₁₀ at various temperatures was determined using synchrotron Xray single crystal diffraction at NSF's ChemMatCARS at Argonne National Laboratory. At room temperature, CsClCu₅P₂O₁₀ crystallizes in the trigonal space group P3m1 (no. 164) with lattice parameters of a = b = 6.1139(1) Å and c= 8.1433(3) Å and Z = 1 (Table S1). These lattice parameters are smaller than those of Rietveld refinement from powder diffraction (see Table S3), which is likely due to the zero shift in the single crystal diffraction at 15-ID-D. Figure 1b shows the crystal structure of CsClCu₅P₂O₁₀ at room temperature by using the ball-and-stick model. There are two Cs atoms, two Cu atoms, one Cl atom, one P atom, and three O atoms in the asymmetric unit. Cs atoms are surrounded by 12 oxygen atoms and 2 Cl atoms, and Cs atoms are disordered with an occupancy of 0.59(11) for Cs1 at (0, 0, 1) and 0.21(5) for Cs2 at (0, 0, 0.946(3)). There are two types of local environments for Cu: one (Cu1) is coordinated by four O atoms with a bond length of 1.8340(9)-2.002(2) Å (planar environment) and the other (Cu2) is surrounded by five O atoms with a bond length in the range of 1.822(4)-2.131(3) Å (trigonal bipyramids). The P atom is coordinated by four O atoms, forming a tetrahedra with P-O bond distances in the range of 1.485(4)-1.523(3) Å (Table S2). The four-coordinated Cu1 atoms form a kagome lattice in the ab plane with a Cu-Cu distance of 3.05695(5) Å (Figure 1c), and the five-coordinated Cu2 atoms form triangles with a Cu-Cu distance of 6.11390(11) Å (Figure 1d). The Cu1 on each triangle is connected to Cu2 with Cu1-Cu2 = 2.9301(5) Å, forming triangle-kagometriangle trilayers (Figure 1e). These trilayers stagger along the c direction, with 3.4656 Å between adjacent trilayers, forming a quasi-2D structure with O, Cs, and Cl for charge balance.

The diffraction data collected at 200 and 100 K reveal a different symmetry compared to that at room temperature. The mean |E²-1| values are 0.815 and 0.666 for 200 and 100 K, respectively. These two values are closer to 0.736 (0.968 expected for the centrosymmetric structure vs 0.736 for noncentrosymmetric), suggesting a noncentrosymmetric struc-

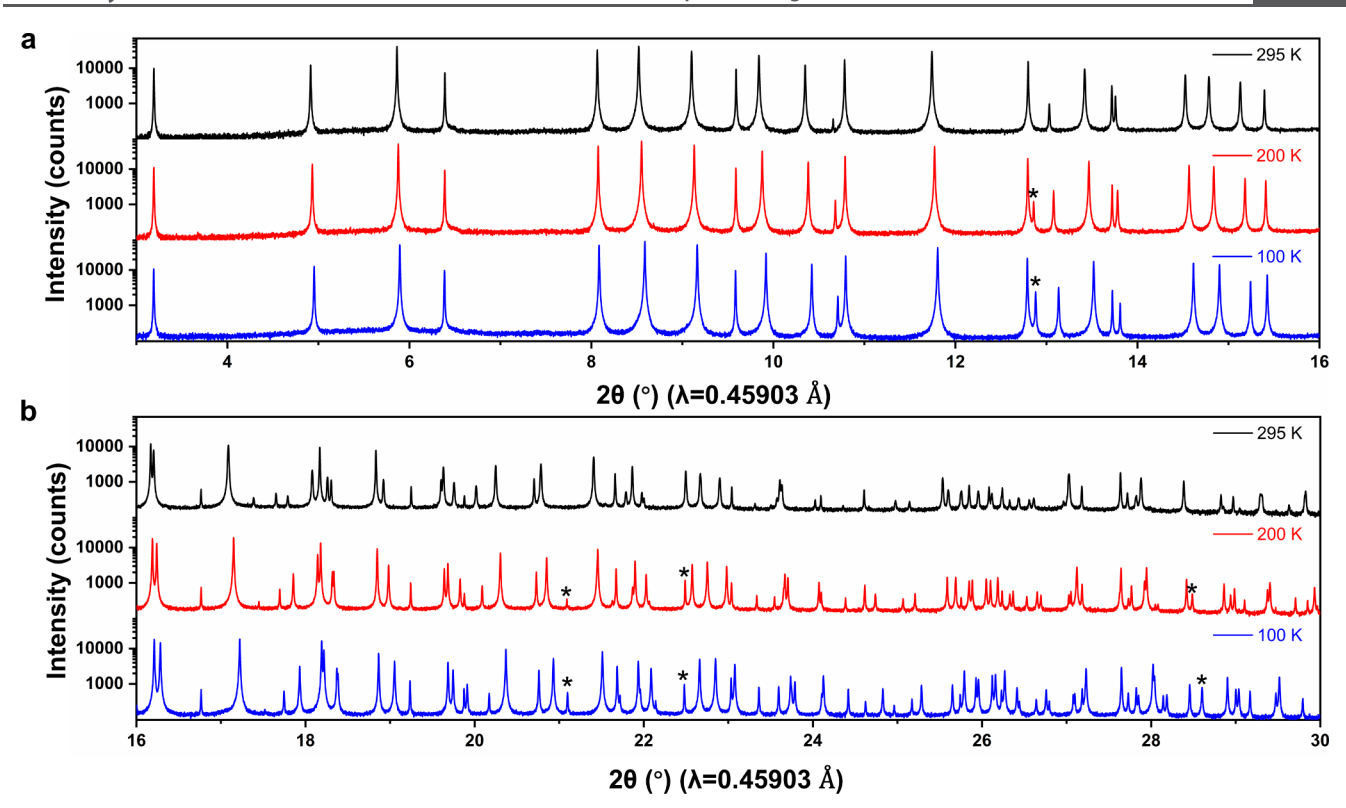


Figure 2. Structural transition of CsClCu₅P₂O₁₀. (a) High-resolution synchrotron X-ray powder diffraction pattern of CsClCu₅P₂O₁₀ in the 2θ range of 3–16° measured at 100, 200, and 295 K. (b) Diffraction pattern in the 2θ range of 16–30° measured at 100, 200, and 295 K. The * indicates peaks shown at 200 and 100 K but not at 295 K.

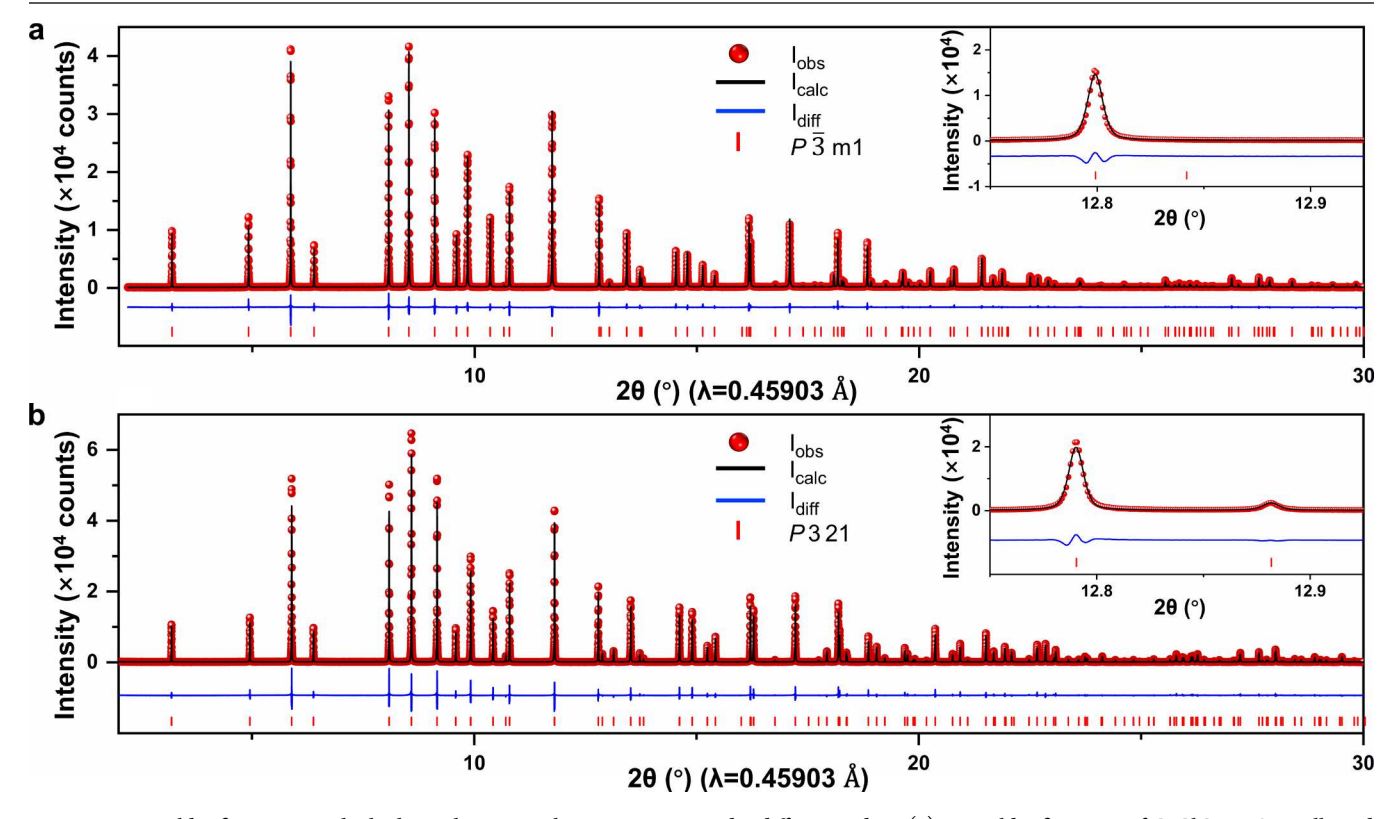


Figure 3. Rietveld refinement on the high-resolution synchrotron X-ray powder diffraction data. (a) Rietveld refinement of $CsClCu_5P_2O_{10}$ collected at 295 K in the 2θ range of $2-30^\circ$ using $P\overline{3}m1$. (b) Rietveld refinement of $CsClCu_5P_2O_{10}$ collected at 100 K in the 2θ range of $2-30^\circ$ using P321.

ture. By lowering symmetry from $P\overline{3}$ m1, P3 and P321 are two possible candidates, and their combined figures of merit are

low (the lower this value, the better the collected data set). The structures at 200 and 100 K were solved using both P3

and P321. Considering the smaller R_1 and higher symmetry of P321, we chose this symmetry to describe the structure at 200 and 100 K (Table S4).

At 100 K, the symmetry of CsClCu₅P₂O₁₀ is lowered and characterized by noncentrosymmetric space group P321 (no. 150). The asymmetric unit contains two Cs atoms, two Cu atoms, one Cl atom, one P atom, and three O atoms. Cu1 is still coordinated by four oxygen atoms; however, Cu1 and the four oxygen atoms no longer lie in the same plane (Figure 1f). The Cu1 atoms in the ab plane form a distorted kagome lattice with Cu-Cu-Cu angles of 100.55(5)° and 139.45(5)° and a distance of 3.0799(3) Å between the nearest Cu1 atoms (Figure 1f). The distortion increases with decreasing temperature, and angles of $97.256(14)^{\circ}$ and $142.744(14)^{\circ}$ are obtained at 6 K (Figure S3). Cu2 is surrounded by five oxygen atoms to form trigonal bipyramids (Figure 1g). Cu1-O, Cu2-O, and P-O polyhedra form a trangle-distorted kagome-trangle trilayer, and these trilayers stagger along the c direction (Figure 1h) to form a quasi-2D structure with Cs and Cl for charge balance.

First-Order Structural Transition. The structural transition between 300 and 100 K is reported here for the first time. High-resolution synchrotron powder X-ray diffraction data were collected at 11-BM at the Advanced Photon Source, Argonne National Laboratory, to verify the existence of a structural transition. **Figure 2** shows the variable temperature diffraction data in the range of 3.0–30.0°. Clearly, extra diffraction peaks are observed at 200 and 100 K, indicating a lower symmetry compared with 295 K. **Table S5** lists selected diffraction peaks calculated from single crystal structural models. Such a structural transition occurring between 295 and 200 K has not been reported previously, and an asymmetric peak shape is observed at 200 and 100 K, which is consistent with the previous report by Winiarski et al.²¹

Figure 3a shows the Rietveld refinement of powder diffraction data collected at 295 K using the single crystal structural model as a starting point. The Rietveld refinement converged to $R_{\rm wp}=8.76\%$ and GOF = 1.48 with lattice parameters of a=b=6.179572(10) and c=8.236771(6) Å. The obtained lattice parameters are consistent with Winiarski et al. Figure 3b shows the Rietveld refinement of data at 100 K using the P321 space group from SXRD, and all peaks are indexed. Rietveld refinement converged to $R_{\rm wp}=11.687\%$ and GOF = 2.15, and the obtained lattice parameters are a=b=6.131495(9) Å and c=8.242389(7) Å. Table S3 summarizes the crystallographic data and Rietveld refinement on the high-resolution synchrotron powder X-ray diffraction data (11-BM, APS) at various temperatures.

X-ray diffraction on single crystals and powders unambiguously demonstrates the existence of a structural phase transition in CsClCu₅P₂O₁₀ on cooling. To further understand at what temperature the transition occurs, we carried out DSC measurements. Figure 4a shows the low-temperature DSC curves between 200 and 250 K. An endothermic peak at 227 K in the heating curve and a corresponding exothermic peak at 223 K in the cooling curve were observed. A pair of endothermic and exothermic peaks in DSC strongly supports that the transition is first order in nature. Figure 4b shows an anomaly at 224 K in specific heat, which is indicative of the presence of a first-order transition. This first-order transition is corroborated by thermal hysteresis in the temperature-dependent magnetic susceptibility data shown in Figure 4c.

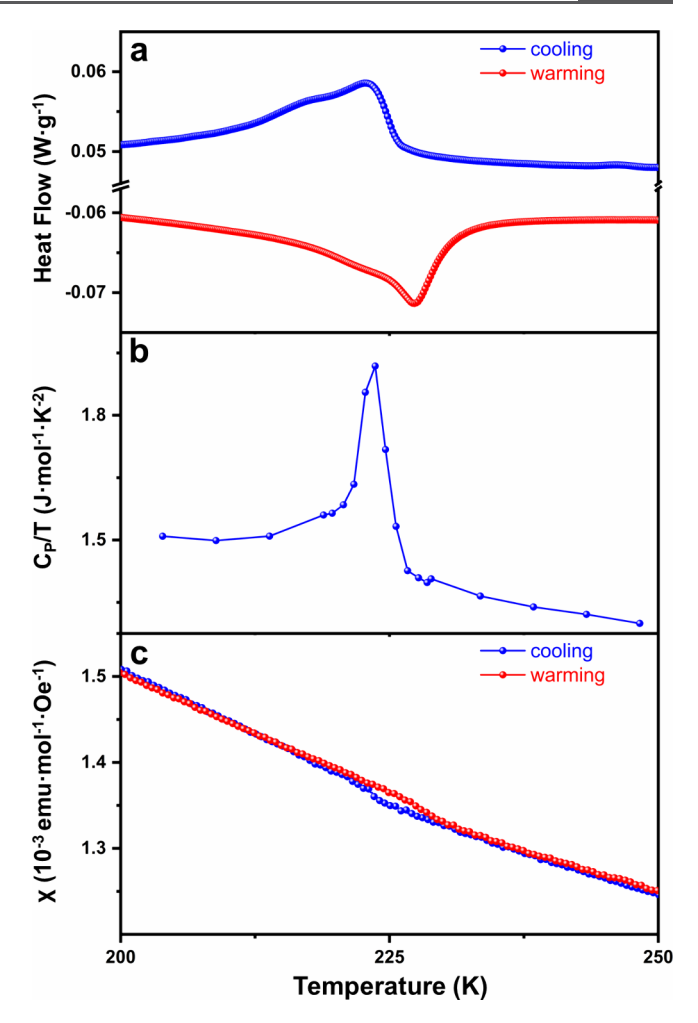


Figure 4. (a) DSC data measured on cooling and warming in the temperature range of 200–250 K. (b) Specific heat data as $C_{\rm P}/T$ measured on cooling in the temperature range of 200–250 K. (c) Magnetic susceptibility in the range of 200–250 K showing thermal hysteresis.

Magnetic Properties with the Magnetic Field Parallel to the ab Plane. Figure 5a shows the in-plane temperaturedependent DC magnetic susceptibility under an applied field of 0.2 T in the temperature range 15-300 K. Curie-Weiss fit in the range 50–200 K leads to $\mu_{\rm eff}$ = 1.99 $\mu_{\rm B}$ and $\theta_{\rm CW}$ = -82 K and $\mu_{\rm eff}$ = 1.74 $\mu_{\rm B}$ and $\theta_{\rm CW}$ = -56 K in the range 230–300 K (Figure S4). The negative Weiss temperature indicates strong antiferromagnetic interactions. For Cu²⁺, the expected effective moment is calculated to be 1.73 μ_B based on $\mu_{cal} = g\sqrt{S(S+1)}$, where spin only S = 1/2 and isotropic Landé g-factor g = 2, and the observed value falls in the range of 1.7–2.2 $\mu_{\rm B}$.³⁰ The obtained effective moments in our case are consistent with the literature. 30 Figure 5b shows the in-plane DC magnetic susceptibility as a function of temperature in the range of 1.8-15 K under magnetic fields of 0.001, 0.01, and 1.0 T (Figure S5). The feature at around 13.6 K is indicative of antiferromagnetic order, and the bifurcation between ZFC and FC at around 8.9 K suggests either ferromagnetic order or spin glass behavior. Preliminary AC magnetic susceptibility data (Figure S6) in the range 10-997 Hz show a peak around 8.9 K, but no apparent frequency dependence is observed. The magnetization as a function of applied magnetic field at 1.8 K exhibits a hysteresis loop between -0.057 and 0.057 T (Figure

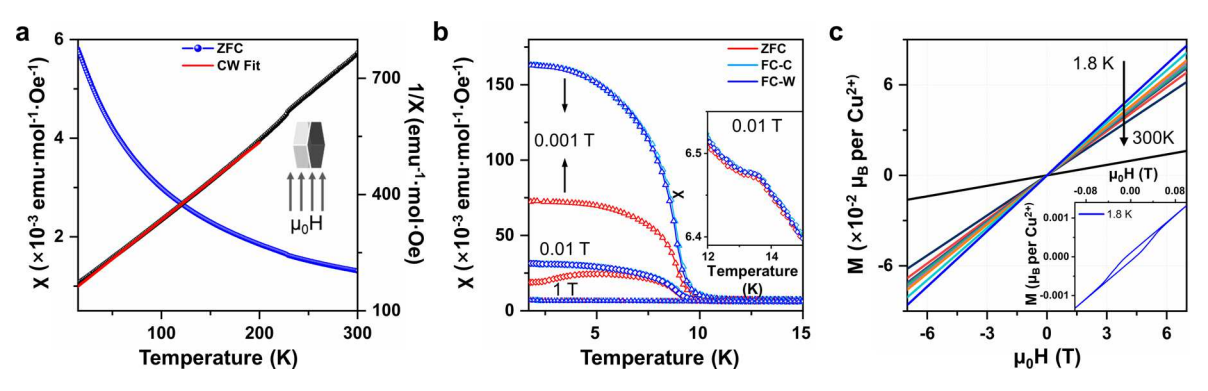


Figure 5. Magnetic properties of $CsClCu_5P_2O_{10}$ with an applied magnetic field parallel to the *ab* plane. (a) Magnetic susceptibility under a magnetic field of 0.2 T. (b) Temperature-dependent DC magnetic susceptibility in the temperature range of 1.8–15 K under applied magnetic fields of 0.001, 0.01, and 1 T. (c) Magnetization as a function of applied magnetic field at various temperatures (1.8, 2, 3, 5, 10, 12, 15, 20, 30, and 300 K).

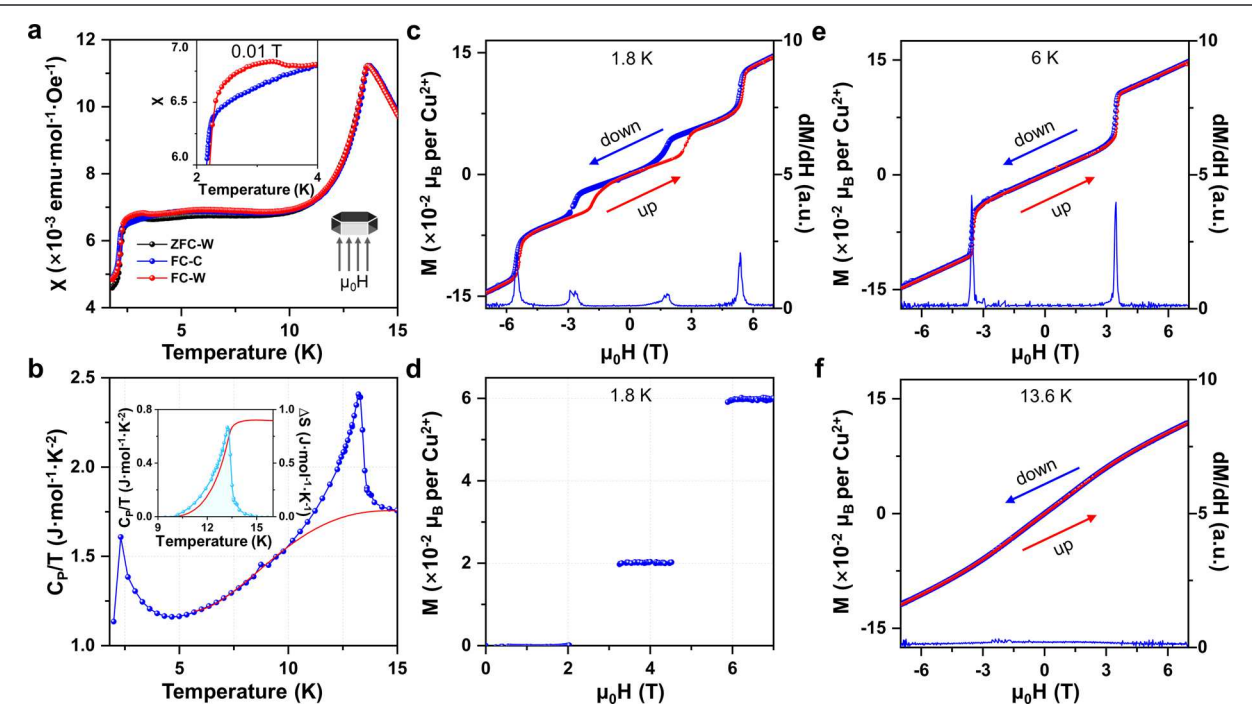


Figure 6. Magnetic properties of $CsClCu_5P_2O_{10}$ with applied magnetic fields perpendicular to the *ab* plane. (a) Temperature dependence of the magnetic susceptibility (ZFC-W, FC-C, and FC-W) at 0.01 T. (b) Specific heat of single crystals in the temperature range 1.8–15 K. (c) Magnetization as a function of magnetic fields (blue: +7 to -7 T, red: -7 to +7 T) at 1.8 K and first-order derivatives of magnetization from +7 to -7 T. (d) Net magnetization with linear components subtracted at 1.8 K, showing two magnetization plateaus. (e) Magnetization as a function of magnetic fields (blue: +7 to -7 T, red: -7 to +7 T) at 6 K and first-order derivatives of magnetization from +7 to -7 T. (f) Magnetization as a function of magnetic fields (blue: +7 to -7 T, red: -7 to +7 T) at 13.6 K and first-order derivatives of magnetization from +7 to -7 T.

Sc, Figure S7), indicating weak ferromagnetism possibly from canted antiferromagnetism. Figure S8 shows the magnetic phase diagram of $CsClCu_5P_2O_{10}$ with $\mu_0H\|ab$, which consists of three states. The temperature dependence of the magnetization of the anomaly at different magnetic fields serves as a dividing line between state I (antiferromagnetic) and paramagnetic states. The maximum magnetic fields of the hysteresis loop at various temperatures serve as markers to distinguish state I from state II (ferromagnetism). State II may be attributed to canted AFM, the magnetic configuration of which remains to be determined through neutron diffraction.

Magnetic Properties with the Magnetic Field Perpendicular to the *ab* Plane. Figure S9a shows the out-of-plane magnetic susceptibility of CsClCu₅P₂O₁₀ as a function of temperature under an external magnetic field of 0.2

T. Above 15 K, a slope change and thermal hysteresis at around 224 K are observed (Figure 4b). We performed the Curie–Weiss fit (Figure S9b) for temperatures above and below the structural transition at around 224 K: (1) in the range 50–200 K, the fit leads to $\mu_{\rm eff}$ = 1.76 $\mu_{\rm B}$ and $\theta_{\rm CW}$ = -59 K, and (2) in the range 230–300 K, the fit results in $\mu_{\rm eff}$ = 1.89 $\mu_{\rm B}$ and $\theta_{\rm CW}$ = -111 K. The calculated effective moments are all close to the expected value of 1.73 $\mu_{\rm B}$ for Cu²⁺ with S = 1/2. The negative Weiss temperatures indicate strong antiferromagnetic interactions. Note that across the structural transition at ~224 K, the change of Weiss temperature is remarkable, suggesting that the structural change strongly affects the interaction of the magnetic moments out of the ab plane.

Now, we move to a magnetic susceptibility below 15 K. Figure 6a shows the temperature dependence of the magnetic

susceptibility (ZFC-W, FC-C, and FC-W) under 0.01 T in the temperature range of 1.8-15 K (see Figure S9c for magnetic susceptibility under other fields), and Figure S9d presents the first-order derivatives of the corresponding magnetic susceptibility. Three anomalies (13.6, 3.71, and 2.18 K) are observed under 0.001 T. The anomaly at 13.6 K under a magnetic field of 0.001 T is suppressed to 9.55 K under 3 T and then to below 1.8 K under 7 T. The strong response to the magnetic field indicates that this anomaly is of long-range antiferromagnetic order (labeled T_{N1}). The Figure 6a inset shows the temperature dependence of the magnetic susceptibility on warming and cooling in the temperature range of 1.8-5 K under 0.01 T (for other magnetic fields, see Figure S10). A hysteresis between 3.71 and 2.28 K is clearly observed, implying a first-order phase transition. The loop changed to 1.81-5.49 K under 3 T and then to below 1.8 K under 4.5 T. For the third anomaly at 2.18 K, it also exhibits a response to the magnetic field (2.18 K under 0.001 T to below 1.8 K under 2.5 T), indicating another antiferromagnetic transition (labeled T_{N2}). Figure 6b shows the heat capacity data of CsClCu₅P₂O₁₀ in the temperature range of 2-15 K under the zero magnetic field, and Figure S11 shows the heat capacity of powders. Two anomalies (13.6 and 2.15 K) are observed, consistent with the magnetic susceptibility data shown in Figure 6a. The entropy change across the 13.6 K transition is 0.896 J/mol·K, which is far below the expected entropy change of three-dimensional antiferromagnetism of spin 1/2 (0.896/(5R× ln 2) = 3.1%). These data suggest that only a small proportion of the magnetic moments antiferromagnetically orders, which is consistent with the strongly frustrated structure of Cu. A similar phenomenon has been reported in the averievite CsClCu₅V₂O₁₀.²⁴

Magnetization Plateau. Figure 6c shows the out-of-plane magnetization as a function of magnetic field at 1.8 K, and the bottom shows the first-order derivative of the magnetization curve (see Figures S12 and S13 for MH curves at other temperatures). At temperatures higher than 13.6 K (Figure \$13), the magnetization is linear, and no hysteresis is observed, consistent with a paramagnetic state. As the temperature decreases, the magnetization deviates from linear behavior. The field-dependent magnetization exhibits a single step between 13.6 and 5 K (Figures 6e,f and S13) and two steps below 5 K. By subtracting the linear component, two magnetization plateaus were obtained (see Figure 6d and Figures S14-S16). Specifically, magnetization at 1.8 K consists of five parts in the first quadrant: three linear components and two steps. In our system, only a small proportion of the magnetic moments antiferromagnetically orders. The system exhibits a substantial degree of paramagnetic and disordered spins, which contributes to the linear component of the MH. To obtain a ferromagnetic signal, we first fit the linear parts using $M = a\mu_0 H + b$ and then subtract $a\mu_0 H$ from the original data. Similar data analysis has been reported previously. 31-33 Interestingly, the magnetization $M = 0.02 \mu_B$ per Cu²⁺ between 3.2 and 4.7 T (plateau 1) is exactly one-third of $M = 0.06 \mu_{\rm B}$ per Cu²⁺ between 5.9 and 7.0 T (plateau 2). The intercept of the fitted curve on the y-axis in Figure S12a corresponds to the magnetization plateaus. The estimated saturated moment of per Cu²⁺ is $M_S = gS\mu_B = 2 \times 1/2 \ \mu_B = 1.0 \ \mu_B$. The two plateaus M = 0.02 and $0.06 \mu_{\rm B}$ per Cu²⁺ are only 1/50 and 3/50 of the saturated M_S (see Figure 6d), suggesting the existence of two quantum magnetic states. Such small magnetic moments are

consistent with the highly frustrated kagome and triangle lattice

Magnetic Phase Diagram with $\mu_0H\perp ab$ **.** Figure 7 shows the magnetic phase diagram of CsClCu₅P₂O₁₀ with a magnetic

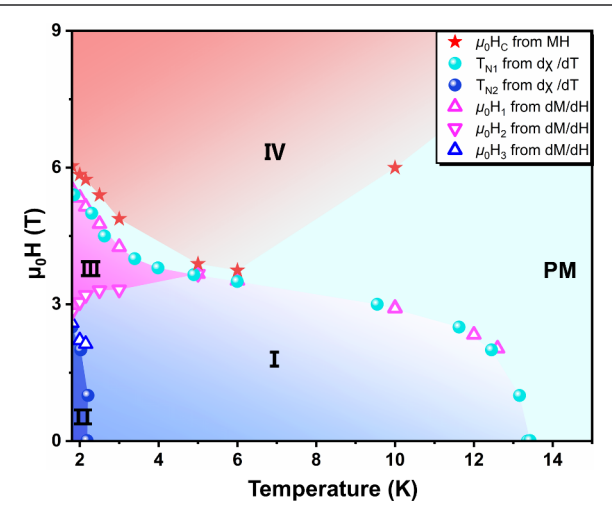


Figure 7. Magnetic phase diagrams of $CsClCu_5P_2O_{10}$ with $\mu_0H\perp ab$.

field perpendicular to the ab plane, summarizing magnetic susceptibility and magnetization data in the temperature range of 1.8-300 K and field range of 0-9 T. As can be seen, the magnetic phase diagram consists of five regions. Under the zero magnetic field, the material exhibits a paramagnetic state at high temperatures; when the temperature is decreased, it undergoes two successive antiferromagnetic transitions at 13.6 and 2.18 K (state I between 13.6 and 2.18 and state II between 2.18 and 1.8 K). At 1.8 K, when an external magnetic field is applied, the material exhibits two metamagnetic transitions, the first starting at ~2.5 T (state III) and the second starting at ~5.5 T (state IV). Above ~6 T, the material likely enters a partially spin polarized state. A fully polarized state may be achieved under a very high magnetic field. 34-36 The boundary between state I and the paramagnetic state can be obtained via T_{N1} , the peak of the first-order derivative of χ . The dividing line between states I (AFM1) and II (AFM2) is T_{N2} . The upper and lower boundaries of state III (Figure S17) are determined by the positions of the peaks in the first-order derivatives of the MH curves μ_0H_1 and μ_0H_2 . The upper limit of III coincides with that of T_{N1}. There is a region between III and IV due to the slopy metamagnetic transitions, as can be seen from the MH curve (Figures 6c,e and S17). The boundary between IV and paramagnetism is determined by the critical magnetic field (μ_0H_C) in the MH curve (Figures S15 and S16). Considering the relatively small magnetic moments, tiny entropy change, and highly frustrated structure, it is challenging to build spin models for different magnetic states. To determine the magnetic structures of CsClCu₅P₂O₁₀ under various magnetic fields, single crystal and/or powder neutron diffraction data are required.

It is well-known that the averievite compounds show structural and magnetic transitions on cooling, 21,24,26,37 for example, two structural transitions and one antiferromagnetic transition were found in polycrystalline V-averievite, 24 and double antiferromagnetic transitions were reported in polycrystalline RbClCu₅P₂O₁₀. However, no study on anisotropic properties has been found. Here, we succeed in growing bulk CsClCu₅P₂O₁₀ single crystals and report for the first time the

large anisotropic magnetic properties and field-induced quantum magnetic states. This is related to the trianglekagome-triangle trilayer, which is a common feature of the averievite family, and the smaller ion size of P.37 It has been reported that the magnetization plateau is the result of the interaction of competing phases in the system from a disorder to an ordered state. For example, 1/6, 1/3, 2/3, and 5/6 plateaus were observed in kagome-lattice HoAgGe. 40 Spingapped solid phases were previously reported at 1/9, 3/9, 5/9, or 7/9 magnetization plateaus due to the crystallization of magnons induced by kinetic frustration. 41,42 Taking the one/ third plateau in the triangular lattice with S = 1/2 for example, the magnetic moment is partially polarized under the magnetic field, forming an "up-up-down" spin structure, so the macroscopic magnetization is expressed as one/third of the saturation magnetic strength.⁴³ For CsClCu₅P₂O₁₀, the magnetization plateau is 1/50 and 3/50 of the saturated moment of Cu^{2+} (S = 1/2), suggesting a different mechanism compared with other common magnetization plateaus (1/6, 1/6)9, 3/9, 5/9, 6/9, 7/9, and 5/6). It is intriguing to explore magnetic plateaus in CsClCu₅P₂O₁₀ under high magnetic fields as well as in other averievite compounds.

CONCLUSIONS

In summary, we report for the first time the cascade of structural and field-induced transitions in quasi-2D averievite CsClCu₅P₂O₁₀ single crystals. A previously unreported structural transition from centrosymmetric P3m1 to noncentrosymmetric P321 was determined by combining synchrotron X-ray single crystal and powder diffraction, differential scanning calorimetry, and magnetic properties. The noncentrosymmetric crystal structure (P321 space group) below the first-order transition in single crystals suggests that the averievite material may have potential applications in the fields of nonlinear optics and piezoelectricity. Large anisotropy was observed in the magnetic properties of CsClCu₅P₂O₁₀ due to the availability of bulk single crystals. A magnetic phase diagram, consisting of a paramagnetic state, two antiferromagnetic states, and two field-induced states including two magnetization plateaus, has been constructed based upon the magnetic susceptibility and magnetization data with a magnetic field perpendicular to the ab plane. CsClCu₅P₂O₁₀ is the first member of the averievite family showing large anisotropic magnetic properties and a rich magnetic phase diagram under external magnetic fields. Determination of the magnetic structures in the phase diagram will require other techniques such as neutron diffraction. It is of great interest to investigate other members of the averievite family, $(MX)_n Cu_5 T_2 O_{10}$ (M =K, Rb, Cs, Cu; X = Cl, Br, I; n = 1; T = P, V). Although CsClCu₅P₂O₁₀ deviates from the long-sought quantum spin liquid state, the substitution of copper in the triangle layers using nonmagnetic ions such as Zn and Mg provided an effective strategy for exploring novel quantum states including quantum spin liquid.

ASSOCIATED CONTENT

Supporting Information

The Supporting Information is available free of charge at https://pubs.acs.org/doi/10.1021/acs.chemmater.4c01342.

Table S1: crystallographic data and refinement parameters for $CsClCu_5P_2O_{10}$ at various temperatures from synchrotron X-ray single crystal diffraction at 15-ID-D,

APS; Table S2: selected bond length and angles for CsClCu₅P₂O₁₀ at various temperatures; Table S3: crystallographic data and Rietveld refinement on the high-resolution synchrotron X-ray powder diffraction data (11-BM, APS); Table S4: crystallographic data for CsClCu₅P₂O₁₀ at 100 K (15-ID-D, APS) using P321 and P3 space groups; Table S5: selected powder diffraction peaks (hkl, I) calculated from single crystal structural models at 300 and 100 K ($\lambda = 0.45903 \text{ Å}$); Figure S1: Xray diffraction patterns of a piece of CsClCu₅P₂O₁₀ single crystal with rectangular (blue) and hexagonal facets (red); Figure S2: magnetic susceptibility and magnetization for different CsClCu₅P₂O₁₀ single crystals; Figure S3: kagome layer consisting of Cu1 at various temperatures; Figure S4: inverse susceptibility $(1/\chi)$ at $\mu_0 H = 0.2$ T and Curie–Weiss fit; Figure S5: temperature-dependent magnetic susceptibility under various magnetic fields (0.001, 1, 3, and 7 T) with the magnetic field parallel to the ab plane; Figure S6: inplane AC magnetic susceptibility at various frequencies and temperatures; Figure S7: magnetization as a function of magnetic field at various temperatures (1.8, 2, 3, 5, 7.5, 10, 12.5, 13.6, and 15 K) with applied magnetic fields parallel to the ab plane; Figure S8: magnetic phase diagram of CsClCu₅P₂O₁₀ with $\mu_0 H \| ab$; Figure S9: magnetic properties of CsClCu₅P₂O₁₀ with applied magnetic fields perpendicular to the ab plane; Figure S10: temperature-dependent magnetic susceptibility under various magnetic fields (0.001, 0.01, 1, 2, 2.5, 3, 3.5, 3.65, 3.8, 4, 4.5, 5, 5.4, and 7 T) with the magnetic field perpendicular to the ab plane; Figure S11: heat capacity of polycrystalline powders and single crystal; Figure S12: magnetization as a function of magnetic field at various temperatures with applied magnetic fields perpendicular to the ab plane; Figure S13: magnetization as a function of magnetic fields at various temperatures with applied magnetic fields perpendicular to the ab plane (-7 T, +7 T) (MPMS3) data); Figure S14: magnetization plateau at 1.8 K $(\mu_0 H \perp ab)$; Figure S15: net magnetization with linear components subtracted for various temperatures with applied magnetic fields perpendicular to the ab plane (MPMS3 data); Figure S16: net magnetization with linear components subtracted for various temperatures with applied magnetic fields perpendicular to the ab plane(PPMS DynaCool-9T data); Figure S17: determination of phase boundaries in the magnetic phase diagram with $\mu_0 H \perp ab$ (DOCX)

AUTHOR INFORMATION

Corresponding Author

Junjie Zhang — State Key Laboratory of Crystal Materials and Institute of Crystal Materials, Shandong University, Jinan, Shandong 250100, China; orcid.org/0000-0002-5561-1330; Email: junjie@sdu.edu.cn

Authors

Chao Liu — State Key Laboratory of Crystal Materials and Institute of Crystal Materials, Shandong University, Jinan, Shandong 250100, China

Tieyan Chang — NSF's ChemMatCARS, The University of Chicago, Lemont, Illinois 60439, United States; ⊚ orcid.org/0000-0002-7434-3714

- Shilei Wang State Key Laboratory of Crystal Materials and Institute of Crystal Materials, Shandong University, Jinan, Shandong 250100, China
- Shun Zhou State Key Laboratory of Crystal Materials and Institute of Crystal Materials, Shandong University, Jinan, Shandong 250100, China
- Xiaoli Wang State Key Laboratory of Crystal Materials and Institute of Crystal Materials, Shandong University, Jinan, Shandong 250100, China
- Chuanyan Fan State Key Laboratory of Crystal Materials and Institute of Crystal Materials, Shandong University, Jinan, Shandong 250100, China
- Lu Han State Key Laboratory of Crystal Materials and Institute of Crystal Materials, Shandong University, Jinan, Shandong 250100, China
- Feiyu Li State Key Laboratory of Crystal Materials and Institute of Crystal Materials, Shandong University, Jinan, Shandong 250100, China
- **Huifen Ren** Synergetic Extreme Condition User Facility (SECUF), Institute of Physics CAS, Beijing 101400, China
- Shanpeng Wang State Key Laboratory of Crystal Materials and Institute of Crystal Materials, Shandong University, Jinan, Shandong 250100, China; orcid.org/0000-0003-2166-0043
- Yu-Sheng Chen NSF's ChemMatCARS, The University of Chicago, Lemont, Illinois 60439, United States

Complete contact information is available at: https://pubs.acs.org/10.1021/acs.chemmater.4c01342

Author Contributions

J.Z. conceived and supervised the project. C.L. grew single crystals and performed in-house powder and single-crystal X-ray diffraction experiments with the help from S.Z., X.W., C.F., L.H., and F.L. C.L. carried out magnetic measurements and single-crystal heat capacity measurements with the help of S.L.W., S.P.W., H.R., and J.Z. T.C. and Y.C. carried out synchrotron X-ray single crystal and powder diffraction measurements. H.R. carried out heat capacity measurements on powders. C.L. and J.Z. analyzed data. C.L. and J.Z. wrote the manuscript with contributions from all coauthors. All authors have given approval to the final version of the manuscript.

Notes

The authors declare no competing financial interest.

ACKNOWLEDGMENTS

J.Z. thanks Prof. Xutang Tao for providing valuable support and fruitful discussions. J.Z. thanks Mr. Mingqi Zhang and Ms. Mengyao Li from Mettler Toledo for their help with lowtemperature DSC measurements. Work at Shandong University was supported by the National Natural Science Foundation of China (12374457 and 12074219), the TaiShan Scholars Project of Shandong Province (tsqn201909031), the QiLu Young Scholars Program of Shandong University, the Crystalline Materials and Industrialization Joint Innovation Laboratory of Shandong University and Shandong Institutes of Industrial Technology (Z1250020003), and the Project for Scientific Research Innovation Team of Young Scholars in Colleges and Universities of Shandong Province (2021KJ093). A portion of this work was carried out at the Synergetic Extreme Condition User Facility (SECUF). NSF's Chem-MatCARS, Sector 15 at the Advanced Photon Source (APS),

Argonne National Laboratory (ANL) is supported by the Divisions of Chemistry (CHE) and Materials Research (DMR), National Science Foundation, under grant number NSF/CHE-1834750. This research used resources of the Advanced Photon Source; a U.S. Department of Energy (DOE) Office of Science user facility operated for the DOE Office of Science by Argonne National Laboratory under contract no. DE-AC02-06CH11357.

■ REFERENCES

- (1) Gui, X.; Lv, B.; Xie, W. Chemistry in Superconductors. *Chem. Rev.* **2021**, *121* (5), 2966–2991.
- (2) Sanders, S.125 Questions: Exploration and Discovery; Science, 2021.
- (3) Keimer, B.; Kivelson, S. A.; Norman, M. R.; Uchida, S.; Zaanen, J. From quantum matter to high-temperature superconductivity in copper oxides. *Nature* **2015**, *518* (7538), 179–186.
- (4) Anderson, P. W. Resonating valence bonds: a new kind of insulator? *Mater. Res. Bull.* 1973, 8 (2), 153–160.
- (5) Anderson, P. W. The resonating valence bond state in La₂CuO₄ and superconductivity. *Science* **1987**, 235 (4793), 1196–1198.
- (6) Kivelson, S.; Sondhi, S. 50 years of quantum spin liquids. *Nat. Rev. Phys.* **2023**, *5*, 368–369.
- (7) Broholm, C.; Cava, R. J.; Kivelson, S. A.; Nocera, D. G.; Norman, M. R.; Senthil, T. Quantum spin liquids. *Science* **2020**, 367 (6475), No. eaay0668.
- (8) Chamorro, J. R.; McQueen, T. M.; Tran, T. T. Chemistry of Quantum Spin Liquids. Chem. Rev. 2021, 121 (5), 2898-2934.
- (9) Lancaster, T.Quantum spin liquids. 2023, Preprint at https://arxiv.org/abs/2310.19577.
- (10) Zhou, Y.; Kanoda, K.; Ng, T.-K. Quantum spin liquid states. *Rev. Mod. Phys.* **2017**, 89 (2), No. 025003.
- (11) Wen, J.; Yu, S. L.; Li, S.; Yu, W.; Li, J. X. Experimental identification of quantum spin liquids. npj Quantum Mater. 2019, 4,
- (12) Ma, Z.; Ran, K.; Wang, J.; Bao, S.; Cai, Z.; Shangguan, Y.; Si, W.; Wen, J. Experimental Progress of Quantum Spin Liquids. *Prog. Phys.* **2019**, 39 (5), 153–172.
- (13) Norman, M. R.; Laurita, N. J.; Hsieh, D. Valence bond phases of herbertsmithite and related copper kagome materials. *Phys. Rev. Research* **2020**, 2 (1), No. 013055.
- (14) Clark, L.; Abdeldaim, A. H. Quantum Spin Liquids from a Materials Perspective. *Annu. Rev. Mater. Res.* **2021**, *51*, 495–519.
- (15) Norman, M. R. Herbertsmithite and the search for the quantum spin liquid. *Rev. Mod. Phys.* **2016**, 88 (4), No. 041002.
- (16) Mazin, I. I.; Jeschke, H. O.; Lechermann, F.; Lee, H.; Fink, M.; Thomale, R.; Valentí, R. Theoretical prediction of a strongly correlated Dirac metal. *Nat. Commun.* **2014**, *5*, 4261.
- (17) Guterding, D.; Jeschke, H. O.; Valentí, R. Prospect of quantum anomalous Hall and quantum spin Hall effect in doped kagome lattice Mott insulators. *Sci. Rep.* **2016**, *6* (1), 25988.
- (18) Puphal, P.; Ranjith, K. M.; Pustogow, A.; Müller, M.; Rogalev, A.; Kummer, K.; Orain, J.; Baines, C.; Baenitz, M.; Dressel, M.; Kermarrec, E.; Bert, F.; Mendels, P.; Krellner, C.; et al. Tuning of a kagome magnet: insulating ground state in Ga-substituted Cu₄(OH)₆Cl₂. Phys. Status Solidi B **2019**, 256 (9), No. 1800663.
- (19) Kelly, Z. A.; Gallagher, M. J.; McQueen, T. M. Electron doping a Kagome spin liquid. *Phys. Rev. X* **2016**, 6 (4), No. 041007.
- (20) Kornyakov, I. V.; Vladimirova, V. A.; Siidra, O. I.; Krivovichev, S. V. Expanding the Averievite Family, $(MX)Cu_5O_2(T^{5+}O_4)_2$ $(T^{5+}=P, V; M=K, Rb, Cs, Cu; X=Cl, Br)$: Synthesis and Single-Crystal X-ray Diffraction Study. *Molecules* **2021**, 26 (7), 1833.
- (21) Winiarski, M. J.; Tran, T. T.; Chamorro, J. R.; McQueen, T. M. $(CsX)Cu_5O_2(PO_4)_2$ (X = Cl, Br, I): A Family of $Cu^{2+}S = 1/2$ Compounds with Capped-Kagomé Networks Composed of OCu_4 Units. *Inorg. Chem.* **2019**, 58 (7), 4328–4336.
- (22) Ginga, V. A.; Siidra, O. I.; Firsova, V. A.; Charkin, D. O.; Ugolkov, V. L. Phase evolution and temperature-dependent behavior

- of averievite, $Cu_5O_2(VO_4)_2(CuCl)$ and yaroshevskite, $Cu_9O_2(VO_4)_4Cl_2$. Phys. Chem. Miner. 2022, 49 (9), 38.
- (23) Volkova, L. M.; Marinin, D. V. Antiferromagnetic spin-frustrated layers of corner-sharing Cu_4 tetrahedra on the kagome lattice in volcanic minerals $Cu_5O_2(VO_4)_2(CuCl)$, Na- $Cu_5O_2(SeO_3)_2Cl_3$, and $K_2Cu_5Cl_8(OH)_4\cdot 2H_2O$. J. Phys.: Condens. Matter 2018, 30 (42), 425801.
- (24) Botana, A. S.; Zheng, H.; Lapidus, S. H.; Mitchell, J. F.; Norman, M. R. Averievite: A copper oxide kagome antiferromagnet. *Phys. Rev. B* **2018**, 98 (5), No. 054421.
- (25) Shores, M. P.; Nytko, E. A.; Bartlett, B. M.; Nocera, D. G. A Structurally Perfect S = 1/2 Kagomé Antiferromagnet. *J. Am. Chem. Soc.* **2005**, 127 (39), 13462-13463.
- (26) Biesner, T.; Roh, S.; Pustogow, A.; Zheng, H.; Mitchell, J. F.; Dressel, M. Magnetic terahertz resonances above the Neel temperature in the frustrated kagome antiferromagnet averievite. *Phys. Rev. B* **2022**, *105* (6), No. L060410.
- (27) Dey, D.; Botana, A. S. Role of chemical pressure on the electronic and magnetic properties of the spin-1/2 kagome mineral averievite. *Phys. Rev. B* **2020**, *102* (12), No. 125106.
- (28) Bruker Computer code APEX4 (Bruker Analytical X-ray Instruments); Bruker Inc.: Madison, Wisconsin, USA., 2022.
- (29) Toby, B. H.; Von Dreele, R. B. GSAS-II: the genesis of a modern open-source all purpose crystallography software package. *J. Appl. Crystallogr.* **2013**, *46* (2), 544–549.
- (30) Mugiraneza, S.; Hallas, A. M. Tutorial: a beginner's guide to interpreting magnetic susceptibility data with the Curie-Weiss law. *Commun. Phys.* **2022**, 5 (1), 95.
- (31) Tsukada, I.; Takeya, J.; Masuda, T.; Uchinokura, K. Two-Stage Spin-Flop Transitions in the S = 1/2 Antiferromagnetic Spin Chain BaCu₂Si₂O₇. *Phys. Rev. L* **2001**, *87* (12), No. 127203.
- (32) Matan, K.; Bartlett, B. M.; Helton, J. S.; Sikolenko, V.; Mat'aš, S.; Prokeš, K.; Chen, Y.; Lynn, J. W.; Grohol, D.; Sato, T. J.; Tokunaga, M.; Nocera, D. G.; Lee, Y. S.; et al. Dzyaloshinskii-Moriya interaction and spin reorientation transition in the frustrated kagome lattice antiferromagnet. *Phys. Rev. B* **2011**, 83 (21), No. 214406.
- (33) Gitgeatpong, G.; Suewattana, M.; Zhang, S.; Miyake, A.; Tokunaga, M.; Chanlert, P.; Kurita, N.; Tanaka, H.; Sato, T. J.; Zhao, Y.; et al. High-field magnetization and magnetic phase diagram of α Cu₂V₂O₇. *Phys. Rev. B* **2017**, 95 (24), No. 245119.
- (34) Gong, G.; Su, D.; Sun, Y.; Xu, L.; He, J.; Tian, Z. High-field magnetization and magnetodielectric effect in a Ni₂NbBO₆ single crystal. *Phys. Rev. B* **2022**, *105* (5), No. 054408.
- (35) Zhu, T.; Zhu, B.; Mentré, O.; Lee, S.; Chen, D.; Jin, Y.; Zhu, W.; Arévalo-López, Á. M.; Minaud, C.; Choi, K.-Y.; et al. Cu₃Te₂O₃(OH)₄: A Frustrated Two-Dimensional Quantum "Magnetic Raft" as a Possible Pathway to a Spin Liquid. *Chem. Mater.* **2023**, 35 (10), 3951–3959.
- (36) Tanaka, H.; Matsuo, A.; Kindo, K. One-half magnetization plateau in the spin-1/2 fcc lattice antiferromagnet Sr₂CoTeO₆. *Phys. Rev. B* **2024**, *109* (9), No. 094414.
- (37) Mohanty, S.; Babu, J.; Furukawa, Y.; Nath, R. Structural and double magnetic transitions in the frustrated spin-1/2 capped-kagome antiferromagnet (RbCl)Cu₅P₂O₁₀. *Phys. Rev. B* **2023**, *108* (10), No. 104424.
- (38) Starykh, O. A. Unusual ordered phases of highly frustrated magnets: a review. Rep. Prog. Phys. 2015, 78 (5), No. 052502.
- (39) Zhitomirsky, M. E.; Honecker, A.; Petrenko, O. A. Field Induced Ordering in Highly Frustrated Antiferromagnets. *Phys. Rev. Lett.* **2000**, 85 (15), 3269–3272.
- (40) Zhao, K.; Deng, H.; Chen, H.; Ross, K. A.; Petříček, V.; Günther, G.; Russina, M.; Hutanu, V.; Gegenwart, P. Realization of the kagome spin ice state in a frustrated intermetallic compound. *Science* **2020**, 367 (6483), 1218–1223.
- (41) Nishimoto, S.; Shibata, N.; Hotta, C. Controlling frustrated liquids and solids with an applied field in a kagome Heisenberg antiferromagnet. *Nat. Commun.* **2013**, *4* (1), 2287.
- (42) Jeon, S.; Wulferding, D.; Choi, Y.; Lee, S.; Nam, K.; Kim, K. H.; Lee, M.; Jang, T.-H.; Park, J.-H.; Lee, S.; et al. One-ninth

magnetization plateau stabilized by spin entanglement in a kagome antiferromagnet. Nat. Phys. 2024, 20 (3), 435–441.

(43) Shangguan, Y.; Bao, S.; Dong, Z.-Y.; Xi, N.; Gao, Y.-P.; Ma, Z.; Wang, W.; Qi, Z.; Zhang, S.; Huang, Z.; et al. A one-third magnetization plateau phase as evidence for the Kitaev interaction in a honeycomb-lattice antiferromagnet. *Nat. Phys.* **2023**, *19*, 1883–1889.